

Numerical simulation of ejected molten metal-nanoparticles liquefied by laser irradiation: Interplay of geometry and dewetting

S. Afkhami and L. Kondic

*Department of Mathematical Sciences and Center for Applied Mathematics and Statistics,
New Jersey Institute of Technology, Newark, NJ 07102 USA*

(Dated: January 13, 2019)

Metallic nanoparticles, liquefied by fast laser irradiation, go through a rapid change of shape attempting to minimize their surface energy. The resulting nanodrops may be ejected from the substrate when the mechanisms leading to dewetting are sufficiently strong, as in the experiments involving gold nanoparticles [Habenicht et al., *Science* **309**, 2043 (2005)]. We use a direct continuum-level approach to accurately model the process of liquid nanodrop formation and the subsequent ejection from the substrate. Our computations show a significant role of inertial effects and an elaborate interplay of initial geometry and wetting properties: e.g., we can control the direction of ejection by prescribing appropriate initial shape and/or wetting properties. We validate our computations by comparing directly with the experiments specified above involving the length scales measured in hundreds of nanometers, and with molecular dynamics simulations on much shorter scales measured in tens of atomic diameters, as in M. Fuentes-Cabrera et al., *Phys. Rev. E* **83**, 041603 (2011). The quantitative agreement, in addition to illustrating the possibility of controlling particle ejection, suggests utility of continuum-based simulations in describing dynamics on nanoscale quantitatively, even in a complex setting as considered here.

PACS numbers: 47.11.-j,68.08.-p,81.16.Rf,68.55.-a

Evolution of fluid drops deposited on solid substrates has been a focus of large research effort for decades. More recently, this effort has been particularly extensive on nanoscale, due to relevance of nanostructures in a variety of fields, ranging from DNA sequencing to plasmonics [1, 2], nanomagnetism [3], and liquid crystal displays and solar panel designs [4]. For example, the size and distribution of metallic particles strongly affects the coupling of surface plasmons to incident energy [1]. Controlling this coupling has the potential for large increases in the yield of solar cell devices.

In addition to physical experiments, modeling and simulations provide a significant insight into the effects governing the evolution of drops and other liquid structures. Simulations have an advantage of allowing to switch off some of the involved physical phenomena and therefore isolate the dominant ones. On nanoscale, however, it is not trivial to decide on appropriate simulation technique. Molecular dynamics (MD) simulations, while very powerful and presumably as close to real physical picture as it is our knowledge of underlying interaction laws, are still extremely computationally demanding - simulating the dynamics of just 100^3 nm of a fluid on a substrate is beyond the reach of most of currently existing computers. Therefore, one would like to resort to continuum simulations. However, it is not immediately clear that this approach is appropriate on nanoscale where the basic assumptions of continuum fluid mechanics are pushed to their limits. In addition, continuum simulations of free surface time-dependent problems based on full Navier-Stokes (N-S) formulation are still computationally demanding. For this reason, this type of simulations is rarely attempted in practice and instead the researchers

resort to asymptotic (long-wave) methods, which allow to reduce the dimensionality and lead to computationally manageable formulations. Such an approach has been applied with success to problems involving wetting and dewetting of drops and films; see [5] for extensive reviews. This direction is, however, questionable not only due to concerns about validity of continuum fluid mechanics, but also due to the assumptions inherent in the long-wave approach, in particular when contact angles are large and inertial effects are significant. One class of problems where these concerns are particularly strong involves liquid metals. These configurations may even lead to topological changes under liquefaction with metal particles detaching from the substrate [6]. In such cases, long-wave theory clearly cannot be applied.

In this work, we show that direct numerical solutions of N-S equations lead to the results which are in quantitative agreement with (i) MD simulations of dewetting of 1 – 1.5 nm thick, liquid copper (Cu) disks of radius of 10–15 nm, and (ii) physical experiments involving ‘jumping’ gold (Au) nanoparticles of typical in-plane length scale in the range of 100 nanometers. While utility of continuum mechanics on nanoscale problems involving liquid metals was discussed previously (see, e.g., [7]), as far as the authors are aware, this is the first attempt to compare explicitly continuum N-S simulations both to MD and to physical experiments in a dynamic setting. Furthermore, we utilize the simulations to illustrate the dominant effects and discuss in particular the conditions leading to ejection of fluid material from the substrate. We first consider dewetting of liquid Cu disks recently simulated by MD [8] and then shift focus to Au particles considered experimentally [6].

Methods. The simulations are based on the Volume of Fluid (VoF) approach, which, when coupled to a flow solver, is also used to compute quantities related to surface tension that enter the flow calculation. Until recently, the VoF method was not deemed appropriate for the study of phenomena in which surface tension is the driving force. Recent improvements to calculating curvature and applying the surface tension force appear to resolve this issue [9]. Within this approach, one solves the three-dimensional N-S equations that govern the motion of the fluid both inside of the liquid domain, and in the surrounding gas phase. For Cu disk structures, a free-slip boundary condition is specified at the substrate; this choice is motivated by the MD simulations [8]. This assumption is also consistent with the fact that the length scale associated with slip is nanometric for most systems [10]. When considering Au structures, the Navier slip [11] with slip length of 3 nm is imposed; this particular value is obtained by direct comparison with the experiments [6] and is further discussed in Supplementary Materials [15]. Such a value is also consistent with the MD simulations [12], indicating slip lengths of a few nanometers for mesoscopic systems. The physical problem considered is the one of a Newtonian, isothermal, incompressible fluid and therefore in the present work we do not consider the effects related to phase change and/or thermal variation of material properties occurring in experiments [6]. Simulations are carried out on an adaptive mesh [13], and numerical convergence has been verified by considering simulations with different grid resolutions [14]. More details about the simulations and material parameters used are given in [15].

Results. Figure 1(a) shows the evolution of a Cu disk of initial height $h_0 = 15 \text{ \AA}$ and radius $R_0 = 150 \text{ \AA}$, for the equilibrium contact angle $\theta_{\text{eq}} = 80^\circ$, which dewetts and collapses into a spherical cap. Figure 1(b) and (c) show the front position, $R(t)$, and velocity, $\dot{R}(t)$, respectively. We also plot the results of MD simulations [8] obtained using two different Lennard-Jones (LJ) potentials for $R_0 = 150 \text{ \AA}$, and (●) LJ3 and (◆) LJ2 with $h_0 = 10 \text{ \AA}$ and (▲) LJ2 with $h_0 = 15 \text{ \AA}$. These results show that our numerical results and the MD simulations [8] yield fully consistent retraction time scales. We also see that θ_{eq} influences the initial rapid retraction, with larger θ_{eq} leading to faster dynamics for early times.

A different type of evolution occurs if θ_{eq} is further increased. To illustrate this, Fig. 2(a) shows snapshots of the profiles for $h_0 = 15 \text{ \AA}$, $R_0 = 150 \text{ \AA}$, and $\theta_{\text{eq}} = 140^\circ$. For this θ_{eq} , the contraction is so fast that the nanodrop jumps off the surface, following elongation in the y direction (normal to the substrate). Similar behavior is observed for any $\theta_{\text{eq}} \gtrsim 130^\circ$, again in quantitative agreement with the MD simulations [8]. The influence of the contact angle on the retraction time and the upward velocity is further discussed in [15].

To gain additional insight regarding the effects that

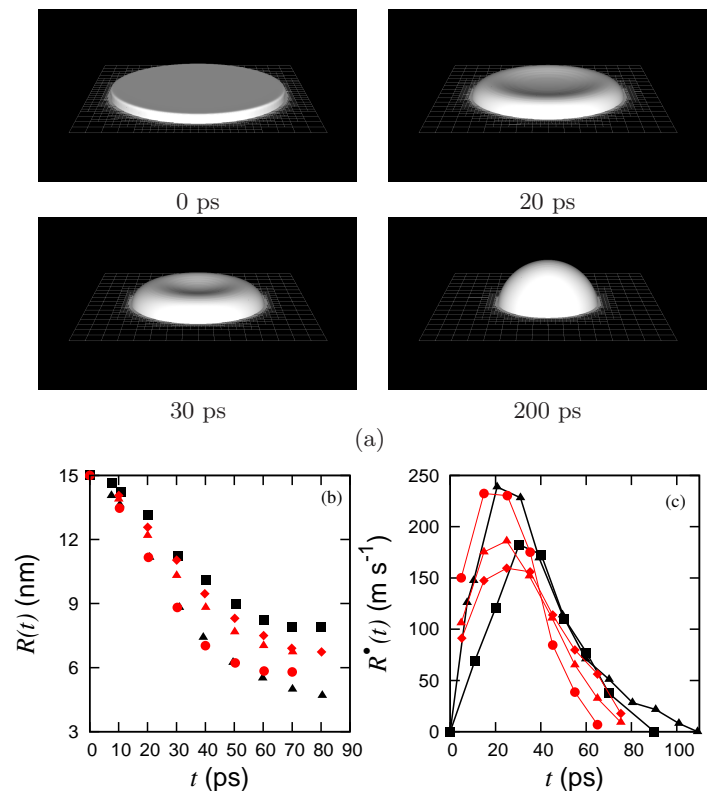


FIG. 1: (Color online) Evolution of a Cu disk ($R_0 = 150 \text{ \AA}$, $\theta_{\text{eq}} = 80^\circ$); (a) Snapshots for $h_0 = 15 \text{ \AA}$; (b) $R(t)$ and (c) $\dot{R}(t)$ for $h_0 = 15 \text{ \AA}$ and (■) $\theta_{\text{eq}} = 80^\circ$ and (▲) $\theta_{\text{eq}} = 115^\circ$. MD simulations for (●) LJ3 and (◆) LJ2 with $h_0 = 10 \text{ \AA}$ and (▲) LJ2 with $h_0 = 15 \text{ \AA}$ [8].

drive contraction, and possibly ejection of the fluid, we have carried out additional set of simulations with reduced inertial effects. This was implemented by reducing incompressible fluid density, but more generally the dynamics can be characterized by Ohnesorge number, $Oh = \eta / \sqrt{\rho \sigma R_0}$, which is related to the Reynolds number defined based on a characteristic capillary velocity, σ / η , as $Re = Oh^{-2}$. For liquid Cu, $Oh \approx 0.35$, suggesting that inertial effects are important; the same conclusion can be reached by considering an intrinsic length scale, $\ell_v = \eta^2 / (\rho \sigma)$, above which inertial effects become significant; for liquid Cu, $\ell_v \approx 1.78 \text{ nm}$, therefore smaller than typical length scales considered here. For the reduced density system, $Oh \approx 1.1$, suggesting that viscosity now dominates over inertia. Figures 2(b) and (c) show $R(t)$ and $\dot{R}(t)$, respectively, for $Oh \approx 0.35$ and $Oh \approx 1.1$. Reduced inertial effects eliminate the most noticeable feature of the dewetting: nanodroplets do not detach from the surface for the same θ_{eq} . Additional simulations have shown that even for $\theta_{\text{eq}} = 150^\circ$ there is no detachment for $Oh \approx 1.1$.

Figure 3 further illustrates the relevance of inertial effects. In Fig. 3(a) ($Oh \approx 0.35$), a capillary ridge formed at the initial stage propagates from the nanodisk rim along the drop-gas interface progressing to the top of the

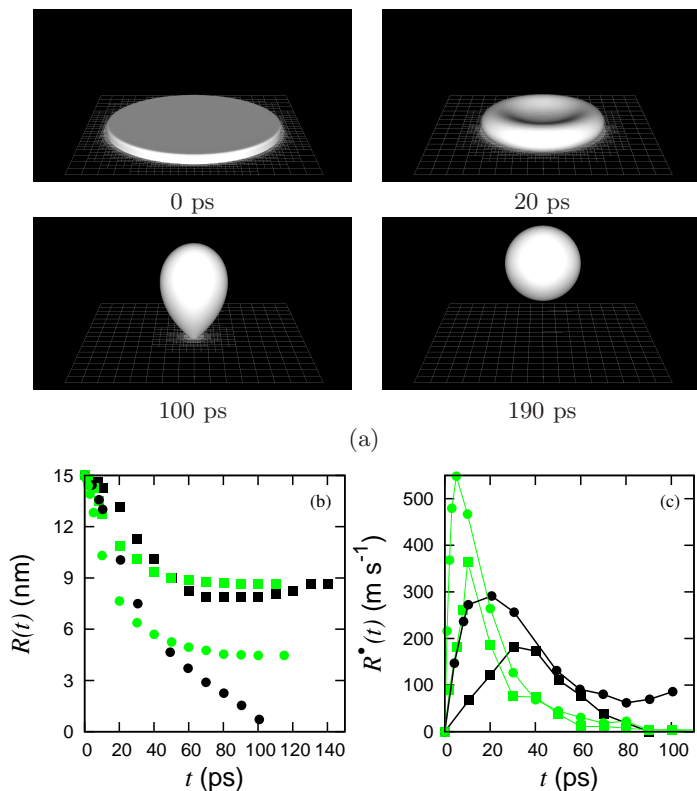


FIG. 2: (Color online) Evolution of a disk ($h_0 = 15 \text{ \AA}$, $R_0 = 150 \text{ \AA}$); (a) for $\theta_{\text{eq}} = 140^\circ$, the disk detaches at around 100 ps (see also animation in [15]); (b) $R(t)$ and (c) $\dot{R}(t)$ for $\theta_{\text{eq}} = 80^\circ$ (■)/(■) and 140° (●)/(●) when $Oh \approx 0.35/Oh \approx 1.1$.

droplet, causing a rapid rise in the droplet height and eventual ejection, while in Fig. 3(b) ($Oh \approx 1.1$), the capillary ridge is less pronounced, leading to a weaker collapse and no ejection.

Next we consider the configuration representative of physical experiments where Au triangular structures were liquefied and let to evolve on SiO_2 substrate [6]. Figure 4 shows snapshots of initially equilateral triangle. The dewetting process first starts at the vertices, where the curvature is high. Due to high surface tension and large θ_{eq} , the fluid starts to accumulate there. The humps at the vertices then coalesce into a droplet. Owing to a low viscosity of liquid gold, inertial effects dominate over viscous dissipation (here $Oh \approx 0.047$ [15]), giving rise to an upward movement that leads to droplet detaching from the surface with a velocity of $\approx 24 \text{ m s}^{-1}$. This process is consistent with the dewetting induced ejection mechanism outlined in [6]. We note the consistency of the time scales found by the simulations and the experiments in [6], where an ejection time scale of the order of 10 ns was observed. In addition to comparing favorably with experiments, the simulations allow for an additional insight since it is possible to explore very fast time scales, and also easily vary the parameters, such as θ_{eq} and the initial shape, and ask what is their influence on the outcome.

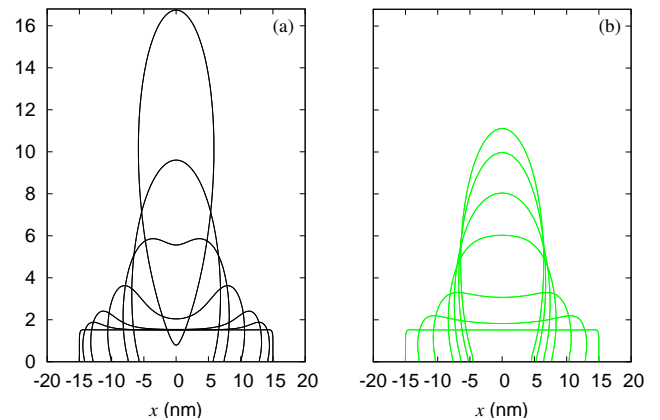


FIG. 3: (Color online) x - y cross sections of a Cu disk ($h_0 = 15 \text{ \AA}$, $R_0 = 150 \text{ \AA}$, $\theta_{\text{eq}} = 140^\circ$) at $t = 0, 5, 10, 20, 30, 40, 110$ ps with (a) $Oh \approx 0.35$ and (b) $Oh \approx 1.1$. The case (a) results in a drop that eventually detaches from the substrate as in Fig. 2(a), while for (b) the final outcome is a sessile droplet; see also Fig. 2(b).

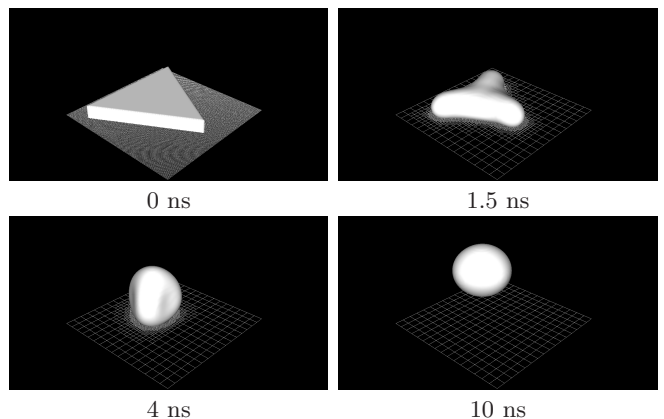


FIG. 4: Evolution of a Au equilateral triangle ($h_0 = 47 \text{ nm}$, $a = 405 \text{ nm}$, and $\theta_{\text{eq}} = 140^\circ$). The structure collapses into a droplet and detaches at $t \approx 7 \text{ ns}$ (see also animation in [15]).

To illustrate the influence of geometry, we consider isosceles triangles. Figure 5 shows a perhaps unexpected result, that despite the fact that the vertex at the smallest angle collapses the fastest due to a higher curvature, the vertices at the larger angles arrive sooner to the center (future work should analyze how general this result is). This mismatch excites oscillations of the droplet translating into a tumbling movement after the ejection.

Next, we ask whether the ejection angle, α , is always $\pi/2$. We find that α can be influenced for asymmetric collapse, and present two means for controlling it by modifying: (i) θ_{eq} and (ii) the initial geometry. Figure 6(a-b) shows that increasing θ_{eq} alters the no-ejection ($\alpha = 0$) to a directional ejection ($0 \leq \alpha \leq \pi/2$). A qualitative understanding can be reached by recalling that $\alpha \neq \pi/2$ due to the lack of synchronicity of the collapse. A larger θ_{eq} results in higher surface energy, speeding up

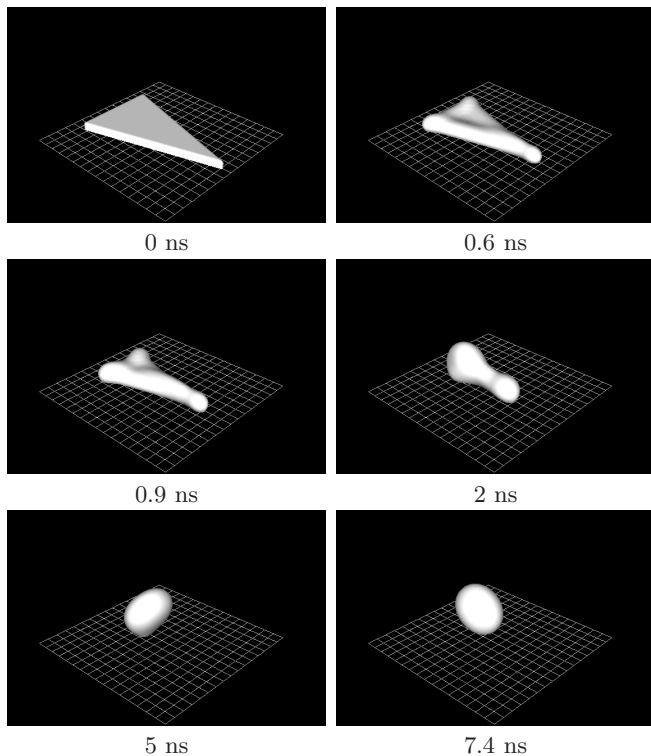


FIG. 5: Evolution of Au isosceles triangle for $h_0 = 24$ nm, long sides $a = 438$ nm and short side $b = 247$ nm ($\theta_{eq} = 140^\circ$). The triangle collapses into a droplet and detaches from the substrate at around 5 ns (see animation in [15]).

the fluid at the vertices. Therefore for larger θ_{eq} , collapse is more synchronous and α is closer to $\pi/2$. For smaller θ_{eq} , α may vanish (see Figure 6(a)), *i.e.* ejection does not happen, while an equilateral triangle with the same θ_{eq} does eject, illustrating the effect of asymmetry. We next consider the aspect ratio of the lengths, (a, b), of triangle sides, and find that the larger a/b ratios lead to increased asymmetry of the collapse and smaller α , as shown in Fig. 6(c-d).

Figures 6(e) and (f) show α versus θ_{eq} for fixed a/b , and versus a/b for fixed θ_{eq} , respectively. In Fig. 6(e) we see that the ejection angle increases monotonically with an increase of θ_{eq} with no ejection for $\theta_{eq} \lesssim 135^\circ$. Figure 6(f) shows that α decreases with increased asymmetry and that for the considered θ_{eq} , the ejection does not occur, *i.e.* $\alpha = 0$, when $a/b \gtrsim 2.4$. Very large ratios lead to a different type of dynamics: Rayleigh-Plateau type of breakup, see [16] for discussion in the context of liquid metals. More elaborate analysis of the influence of geometry and wetting properties is needed to fully understand the dynamics - we leave this for future work.

Conclusions. In this work, we have demonstrated that continuum simulations provide good quantitative agreement with both MD simulations on the length scales in the range of 1–10 nm, and with the physical experiments with in-plane length scales measured in the range of 100 nanometers. We expect that this finding will further mo-

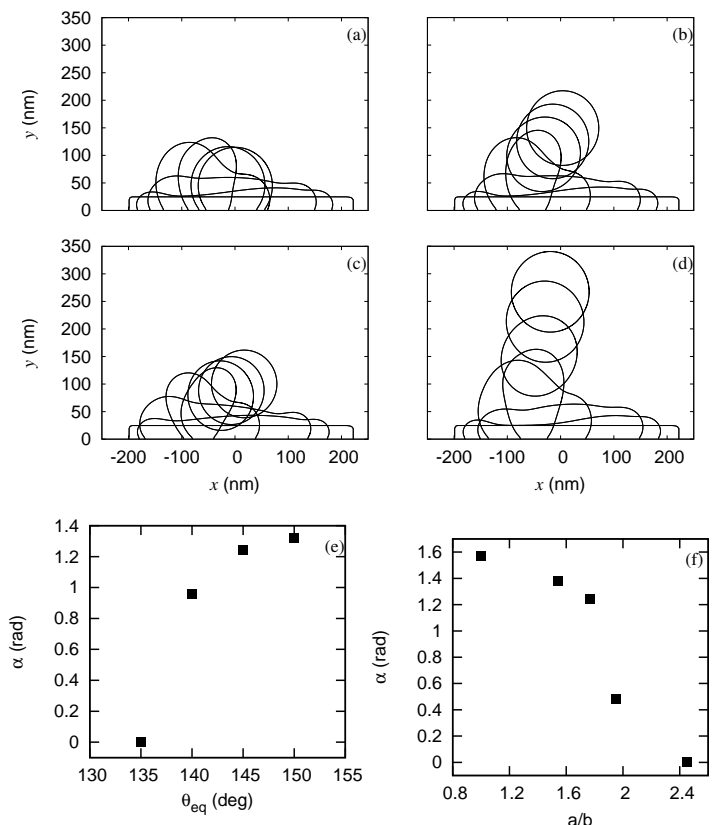


FIG. 6: x - y cross sections of Au isosceles triangles for $h_0 = 24$ nm; (a-b) $a = 438$ nm and $b = 247$ nm for (a) $\theta_{eq} = 130^\circ$, (b) 140° , showing increase of ejection angle, α , as θ_{eq} is increased (note that in (a), $\alpha = 0$); (c-d) $\theta_{eq} = 145^\circ$, and (c) $a = 362$ nm, $b = 185$ nm, (d) $a = 475$ nm, $b = 308$ nm; $t = 0, 0.6, 1.2, 3, 4.4, 11, 19, 35$ ns. (e-f) Ejection angle α versus the θ_{eq} (e), when $a/b \approx 1.77$, and the initial geometrical ratio a/b (f), when $\theta_{eq} = 145^\circ$.

tivate modeling and computational work on these scales, since it is suggesting that continuum simulations have a predictive power. For the problem of dewetting and possibly detaching nanodrops, the simulations provide precise insight regarding the influence of inertial, viscous, and capillary forces, in addition to the liquid/solid interaction. Furthermore, the simulations provide a clear prediction that the direction of ejection of fluid from the substrate can be influenced (and controlled) by modifying either wetting properties or the initial geometry. Future computational and modeling work will include the thermal and phase change effects, allowing to even more accurately model the dynamics of liquid metals on nanoscale.

-
- [1] S. Maier, *Plasmonics: Fundamentals and Applications* (Springer-Verlag, New York, 2007).
 - [2] H. Atwater and A. Polman, *Nat. Mat.* **9**, 9 (2010).
 - [3] S. Baderi, *Rev. Mod. Phys.* **78**, 1 (2006).
 - [4] S. A. Maier et al., *Nat. Mat.* **2**, 229 (2003); S. Sun et al., *Science* **287**, 1989 (2000).
 - [5] A. Oron, S. H. Davis, and S. G. Bankoff, *Rev. Mod. Phys.* **69**, 931 (1997); R. Craster and O. Matar, *Rev. Mod. Phys.* **81**, 1131 (2009).
 - [6] A. Habenicht et al., *Science* **309**, 2043 (2005).
 - [7] J. C. Burton, J. E. Rutledge, and P. Taborek, *Phys. Rev. Lett.* **92**, 244505 (2004).
 - [8] M. Fuentes-Cabrera et al., *Phys. Rev. E* **83**, 041603 (2011).
 - [9] M. Sussman, *J. Comput. Phys.* **187**, 110 (2003); S. Afkhami and M. Bussmann, *Int. J. Numer. Meth. Fluids* **57**, 453 (2008); S. Afkhami and M. Bussmann, *Int. J. Numer. Meth. Fluids* **61**, 827 (2009).
 - [10] D. Bonn et al., *Rev. Mod. Phys.* **81**, 739 (2009).
 - [11] P. J. Haley and M. J. Miksis, *J. Fluid Mech.* **223**, 57 (1991).
 - [12] T. Qian, X.-P. Wang, and P. Sheng, *Phys. Rev. Lett.* **93**, 094501 (2004).
 - [13] S. Popinet, *J. Comput. Phys.* **190**, 572 (2003).
 - [14] S. Afkhami, S. Zaleski, and M. Bussmann, *J. Comput. Phys.* **228**, 5370 (2009).
 - [15] See Supplemental Material including animations at [URL will be inserted by publisher].
 - [16] L. Kondic et al., *Phys. Rev. E* **79**, 026302 (2009); J. D. Fowlkes et al., *Nano Lett.* **11**, 2478 (2011).

SUPPLEMENTARY MATERIAL:

MATHEMATICAL MODEL

The equations of conservation of mass, $\nabla \cdot \vec{U} = 0$, and momentum are written as

$$\frac{\partial}{\partial t}(\rho \vec{U}) + \nabla \cdot (\rho \vec{U} \vec{U}) = -\nabla p + \nabla \cdot \vec{\tau} + \vec{F}_{st}, \quad (1)$$

where $\vec{U} = (u, v, w)$ represents the velocity vector, p the pressure, ρ the fluid density, $\vec{\tau}$ the shear stress tensor, and \vec{F}_{st} the surface tension force (per unit volume) acting on the fluid. The shear stress tensor is defined as $\vec{\tau} = \mu(\nabla \vec{U} + (\nabla \vec{U})^T)$, where μ represents the fluid dynamic viscosity.

The flow equations have been written in an Eulerian frame of reference, and thus a solution of these equations must be coupled with a methodology for following the deforming fluid-fluid interface. Here, the ‘Volume of Fluid’ (VoF) algorithm is implemented [1–3]. Volume tracking requires the introduction of a scalar function f defined as

$$f = \begin{cases} 0 & \text{in fluid 1} \\ 1 & \text{in fluid 2,} \end{cases}$$

for a two fluid system. Since f is passively advected with the flow, it satisfies the advection equation

$$\frac{\partial f}{\partial t} + (\vec{U} \cdot \nabla) f = 0. \quad (2)$$

Density and viscosity are then evaluated via volume-weighted formulae as $\rho = \rho_1 + (\rho_2 - \rho_1)f$ and $\mu = \mu_1 + (\mu_2 - \mu_1)f$, respectively, where subscripts 1 and 2 refer to fluids 1 and 2, respectively.

The surface tension force \vec{F}_{st} in (1) is reformulated as an equivalent volume force [4], which is non-zero only at each interface cell

$$\vec{F}_{st} = \sigma \kappa \delta_S \hat{n}, \quad (3)$$

where σ is a constant interfacial tension and δ_S denotes the Dirac delta function for the surface separating the fluids. The curvature κ and unit normal \hat{n} directed into fluid 1 are geometric characteristics of the surface and are described in terms of f and computed with a second-order ‘height-function’ (HF) method [5–8]. Within the VoF-based sharp surface tension representation, $\delta_S \hat{n}$ is equivalent to ∇f , thus

$$\vec{F}_{st} = \sigma \kappa \nabla f. \quad (4)$$

If partial slip is allowed at the contact line, we impose the Navier slip boundary condition [9] at the (static) solid surface $y = 0$,

$$(u, w)|_{y=0} = \lambda \partial(u, w)/\partial y|_{y=0}, \quad (5)$$

where λ is the slip length. For dynamic contact lines, the Navier slip boundary condition leads to a regularization of the viscous stress singularity at the contact line [9].

	Cu	Au
R_0 (Cu), L_0 (Au)	150 Å	405 nm
L_x, L_y, L_z	375 Å	494 nm
Δ	2.93 Å	1.5 nm
ρ_{air} (kg m ⁻³)	1.225	1.225
η_{air} (kg m ⁻¹ s ⁻¹)	0.00002	0.00002
ρ_{drop} (kg m ⁻³)	7900	17310
η_{drop} (kg m ⁻¹ s ⁻¹)	0.004288 (@ 1500 K)	0.00425 (@ 1500 K)
σ (kg s ⁻²)	1.305	1.15
$Oh = \eta/\sqrt{\rho\sigma L}$	0.35	0.047

TABLE I: Overview of the sets of parameters used in the numerical simulations [10, 11]. Initial conditions are specified in terms of disk radius, R_0 for Cu and a typical length of a triangle side, L_0 for Au. In computing Ohnesorge number, Oh , for the typical length scale, L , we use R_0 for Cu and L_0 for Au.

COMPUTATIONAL MODEL

The main issue is the imposition of the contact angle, described in [3, 7]. Briefly, within our VoF framework, the contact angle boundary condition enters the N-S solver in two ways: it defines the orientation \hat{n} of the VoF interface reconstruction at the contact line, and it influences the calculation of the contact line curvature; together, these two reflect the wettability of the surface. We implement the HF methodology to impose the contact angle in 3D [3]. The HF methodology accurately computes interface curvatures at the contact line, values that converge with mesh refinement. In our HF methodology, the curvature at the contact line is computed at the desired contact angle in order to balance the surface tension forces on the contact line as in Young’s relation: $\sigma \cos \theta_e = \sigma_{sg} - \sigma_{sl}$, where σ_{sg} and σ_{sl} are interfacial tensions for the solid-gas and solid-liquid surfaces, respectively. If the actual contact angle is out of equilibrium, the resulting mismatch in curvature generates a kink in force thus driving the contact line to configuration that satisfies Young’s relation.

COMPUTATIONAL PARAMETERS

Table I provides an overview of the parameter sets used. The computational domain is $L_x \times L_y \times L_z$ and the maximum grid resolution of the adaptive mesh is represented by Δ . For all the simulations, an open boundary condition (pressure and velocity gradient equal zero) is imposed at the top and a symmetry boundary condition is imposed on the lateral sides.

DETERMINATION OF THE APPROPRIATE SLIP LENGTH

We explored the influence of slip length by carrying out numerical experiments for Au structures. Larger slip lengths lead to faster collapse and large detachment velocity. In Fig. 7, we show that by choosing the slip length of 3 nm, the computed detachment velocity of nanostructures compares well with the experimental results from [11]; this value is therefore used in all presented Au simulations.

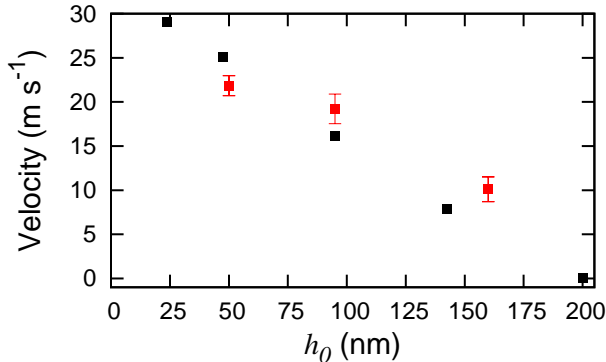


FIG. 7: (Color online) Droplet detachment velocity for liquefied triangular Au nanostructures with a side length of 405 nm and various thicknesses, numerical results (■) and experimental measurements (■). Numerical results are obtained using the slip length of 3 nm.

RETRACTION OF A COPPER DISK

We present the effect of contact angle on the retraction time and the upward velocity of a Cu disk of initial height $h_0 = 15$ Å and radius $R_0 = 150$ Å, for the equilibrium contact angle $\theta_{eq} \geq 130^\circ$. Table II presents the variation

of the retraction time and the upward velocity with θ_{eq} . We find that retraction dynamics is slower for smaller θ_{eq} , while the upward velocity increases for larger θ_{eq} . The computed values are in agreement with the ones obtained in the MD simulations [12].

θ_{eq}	130°	140°	150°
collapse time (ps)	120	100	90
upward velocity (m s ⁻¹)	62	119	137

TABLE II: Effect of contact angle on the retraction time and the detachment velocity.

- [1] C. W. Hirt and B. D. Nichols, *J. Comput. Phys.* **39**, 201 (1981).
- [2] D. Gueyffier, J. Li, A. Nadim, R. Scardovelli, and S. Zaleski, *J. Comput. Phys.* **152**, 423 (1999).
- [3] S. Afkhami and M. Bussmann, *Int. J. Numer. Meth. Fluids* **61**, 827 (2009).
- [4] J. U. Brackbill, D. B. Kothe, and C. Zemach, *J. Comput. Phys.* **100**, 335 (1992).
- [5] M. Sussman, *J. Comput. Phys.* **187**, 110 (2003).
- [6] S. J. Cummins, M. M. Francois, and D. B. Kothe, *Comp. Struct.* **83**, 425 (2005).
- [7] S. Afkhami and M. Bussmann, *Int. J. Numer. Meth. Fluids* **57**, 453 (2008).
- [8] M. M. Francois, S. J. Cummins, E. D. Dendy, D. B. Kothe, J. M. Sicilian, and M. W. Williams, *J. Comput. Phys.* **213**, 141 (2006).
- [9] P. J. Haley and M. J. Miksis, *J. Fluid Mech.* **223**, 57 (1991).
- [10] M. Fuentes-Cabrera, B. Rhodes, M. Baskes, H. Terrones, J. Fowlkes, M. Simpson, and P. Rack, *ACS Nano* **5**, 7130 (2011).
- [11] A. Habenicht, M. Olapinski, F. Burmeister, P. Leiderer, and J. Boneberg, *Science* **309**, 2043 (2005).
- [12] M. Fuentes-Cabrera, B. Rhodes, J. Fowlkes, A. López-Benzanilla, H. Terrones, M. Simpson, and P. Rack, *Phys. Rev. E* **83**, 041603 (2011).